Bimetallic Ions Co-Doped Nanocrystals: Doping Mechanism, Defect Formation and Associated Structural Transition

Qingbo Sun,[†] Changlin Zheng,[‡] Larissa Q. Huston,[§] Terry J. Frankcombe,[∥,*] Hua Chen,[⊥] Chao Zhou,[ᵀ] Zhenxiao Fu,[ᵀ] Ray L. Withers,[†] Lasse Norén,[†] Jodie E. Bradby,[§] Joanne Etheridge,[‡,※] and Yun Liu[†,*]

[†]Research School of Chemistry, [§]Research School of Physics and Engineering, [⊥]Centre for Advanced Microscopy, the Australian National University, Canberra, Australian Capital Territory, 2601, Australia

[‡]Monash Centre for Electron Microscopy, [※]Department of Materials Science and Engineering, Monash University, Victoria, 3800, Australia

[∥]School of Physical, Environmental and Mathematical Sciences, University of New South Wales, Australian Capital Territory, 2601, Australia

[ᵀ]Fenghua Advanced Technology Holding Co., Ltd., Zhaoqing, Guangdong, 526020, China

ABSTRACT: Ionic co-doping offers a powerful approach for modifying material properties by extending the choice of potential dopant ions. However, it has been a major challenge to introduce certain ions that have hitherto proved difficult to use as dopants (called "difficult-dopants") into crystal structures at high concentrations, especially through wet chemical synthesis. Furthermore, the lack of a fundamental understanding of how co-dopants are incorporated into host materials; which types of defect structures they form in the equilibrium state; and what roles they play in material performance, has seriously hindered the rational design and development of promising co-doped materials. Here, we take In^{3+} (difficult-dopants) and Nb^{5+} (easy-dopants) co-doped anatase TiO_2 nanocrystals as an example and investigate the doping mechanism of these two different types of metal ions, the defect formation, and their associated impacts on high-pressure induced structural transition behaviours. It is experimentally demonstrated that the dual mechanisms of nucleation and diffusion doping are responsible for the synergic incorporation of these two dopants, and theoretically evidenced that the defect structures created by the introduced In^{3+}, Nb^{5+} co-dopants, their resultant Ti^{3+} and oxygen vacancies are locally composed of both defect clusters and equivalent defect pairs. These formed local defect structures then act as nucleation centres of baddeleyite- and α-PbO_2-like metastable polymorphic phases and induce the abnormal trans-regime structural transition of co-doped anatase TiO_2 nanocrystals under high pressure. This work thus suggests an effective strategy to design and synthesize co-doped nanocrystals with highly concentrated difficult-dopants. It also unveils the significance of local defect structures on material properties.

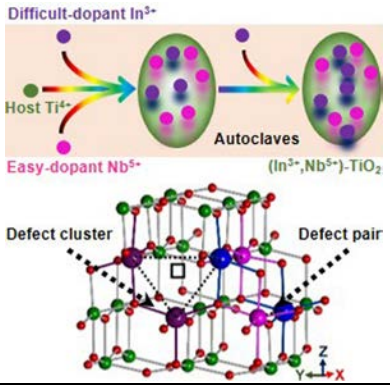

Ionic co-doping is a general and effective strategy to significantly improve the macroscopic performances of host materials by tuning their local and average structures. By simultaneously incorporating two or more types of extrinsic ions into the substitutional or interstitial sites of crystal structures, the physicochemical properties of the host materials, such as their dielectric response, optical absorption or magnetic spin, can be modified significantly. Typical cases can be found in titanium dioxide (TiO_2) due to its multifunctional nature and diverse applications. For instance, our previous work[1] suggested that co-doping In^{3+} and Nb^{5+} ions into rutile TiO_2 ceramics enabled the achievement of both colossal permittivity (over 10^5) and low dielectric loss (less than 5%) as a consequence of the formation of electron pinned defect dipoles. Likewise, the simultaneous incorporation of both B^{3+} and N^{3-} ions into anatase TiO_2 microspheres narrowed the host bandgap and thereby enhanced the visible light photocatalytic activity.[2] Theoretically, Cr and Mn ion co-doping was predicted to greatly increase magnetic moments and thus induced abnormal ferromagnetism in paramagnetic TiO_2.[3] In other material systems including graphene, carbon nanotubes, tetrahedrites and zinc sulfide, the ionic co-doping strategy has also been broadly utilized to improve their electro-catalytic, thermoelectric or fluorescent properties.[4-7]

The ionic co-doping strategy also presents many advantages on the resultant chemical compositions of co-doped materials. Ions, which on their own might be difficult to introduce into host materials, can be co-doped at significantly higher concentrations due to the generation of synergistic effects with another dopant ion. For instance, less than 1 at.% In^{3+} ions can be dissolved into TiO_2 without phase segregation,[8] whereas the dissolution limit can approach ~5 at.% if co-doped with Nb^{5+} ions.[1] Under some scenarios, unwanted species such as oxygen vacancies in the case of N^{3-} single-doped TiO_2[9] or Ti^{3+} ions in the case

of Nb^{5+} mono-doped TiO_2,[10] which lead to a deterioration of photocatalytic properties by forming "trapping or recombination centers" of photo-generated electron-hole pairs, can also be efficiently avoided if another appropriate ion is introduced to couple with each other as well as to balance the overall charge of the whole co-doped system (*e.g.* Nb^{5+}-N^{3-} co-doping).[11]

From a structural perspective, ionic co-doping also changes the local structures of the host materials. The selected co-doped ions can exist as isolated point defects, bind together to form defect pairs or form larger local defect clusters[1,5,12-14] depending upon the chemical compositions or synthesis route. We previously pointed out that co-doping "too big" trivalent In^{3+} ions with Nb^{5+} ions was favorable to generate triangular- and diamond-shaped defect clusters in rutile TiO_2[1] while co-doping smaller Al^{3+} ions with Nb^{5+} ions locally produced an intergrown, intermediate and metal ion rich structure.[15] In (B, N) co-doped carbon nanotubes,[5] the B^{3+} and N^{3-} ions could either exist as isolated point defects or chemically bind together depending on their synthesis conditions. The resultant electrocatalytic properties of prepared (B, N) co-doped carbon nanotubes, however, could only be enhanced by the former.

Though ionic co-doping has been successfully used to tune the physicochemical properties of a wide range of host materials by slightly modifying the chemical composition or locally creating different defect states, their reliable wet chemical synthesis remains complicated and rather difficult to control. This is especially the case when the ions that are difficult to dope with (called "difficult-dopants") are involved since (1) the solubility of the initial reactants should be considered to guarantee enough ions to homogeneously distribute in the reaction solvent; (2) the precipitation of co-dopant ions should be coordinated to inhibit the generation of possible impurities during the reaction process; and (3) the ligands of the metal ions should be modified to achieve the expected doping concentrations in the resultant products. Furthermore, fundamental concerns regarding the synthesis and the resultant co-doped materials themselves still remain unclear, *e.g.* how are co-dopants introduced into the crystal structures of host materials during the chemical reaction process (*i.e.* doping mechanism); whether the same types of co-dopants create the same defect states in different polymorph of the same material (*i.e.* defect formation); and what roles these introduced local defect structures play on the macroscopic properties of the co-doped host materials. Studies on the doping mechanism, the defect formation and their associated impacts are rather important to both design and synthesize novel types of co-doped materials as well as further understand the intrinsic structure-performance relationship.

We herein combine the easy- and difficult-dopant ions together in an attempt to effectively increase the doping levels of the latter. In^{3+} and Nb^{5+} co-doped anatase nanocrystals are then synthesized to further demonstrate the effectivess of the designed co-doping stategies. The potential doping mechanisms of the two different types of metal ions (the In^{3+} difficult-dopant ions and the Nb^{5+} easy-dopant ions) are investigated under solvothermal reaction conditions. Through density functional theory (DFT) calculations, we present the local defect structures generated by the In^{3+}, Nb^{5+} co-dopants, the resultant Ti^{3+} ions and oxygen vacancies. Furthermore, the influence of these intentionally introducted local defect structures on high pressure reaction behaviours of synthesized co-doped nanocrystals are analyzed.

In^{3+} and Nb^{5+} co-doped anatase nanocrystals with a chemical formula of $(Ti^{4+}_{1-x-y-z}Ti^{3+}_{x}In^{3+}_{y}Nb^{5+}_{z})(O^{2-}_{2-(x+y-z)/2}\square_{y/2})$ are synthesized by a solvothermal method ($\square$ here represents oxygen vacancies and also labelled as $V_O^{\cdot\cdot}$). The x, y and z values in the above chemical formula are experimentally determined to range from 0 up to 0.046 and are controlled by adjusting the concentrations of niobium pentachloride and indium acetate in ethanol solvent while fixing the added volume of titanium chloride. Detailed descriptions about the synthesis and characterization of these nanocrystals are given in the supporting information (SI-1 and SI-2). In^{3+} and Nb^{5+} ions are chosen as appropriate co-dopant ions since they enable charge compensating as well as produce a significant local structural change due to the bigger ionic radii of both co-dopants (94 pm for In^{3+} and 78 pm for Nb^{5+}) as compared to that of Ti^{4+} (74.5 pm). Such local structural variation induced the formation of defect clusters in the case of the analogous (In^{3+}+Nb^{5+}) co-doped rutile TiO_2 ceramics[1] to "pin" electrons and thus resulted in an excellent dielectric performance.

In the current anatase case, the ionic radii of the In^{3+} ions are again significantly too large. The calculated apparent valence (AV) or bond valence sum (BVS), of an In^{3+} ion in anatase TiO_2 is 5.33 valence units (v.u.) instead of the ideal 3.00 v.u. estimated using the softBV program (SI-3, supporting information),[16-18] *i.e.* about 78% over-bonded! Without the removal of at least one of the surrounding oxygen ions and the addition of a further neighboring In^{3+} ion for charge balance, it is rather difficult to introduce In^{3+} ions into TiO_2 to achieve high doping levels by normal wet chemical reaction routes such as sol-gel or co-precipitation. A solvothermal method is thus attempted to combine the higher spontaneous pressure of ethanol with the comparatively higher heating temperature of sealed autoclaves. In contrast to the difficulty in In^{3+} doping, the ionic radii of Nb^{5+} ions are almost similar to that of Ti^{4+} with an AV of 5.37 v.u., only slightly over-bonded by ~7.4% (SI-3, supporting information). The chemical doping of Nb^{5+} ions into anatase TiO_2 is thus relatively easy and can reach up to a concentration of about 14 at.%[19] or more (called "easy-dopants"). Note, however, that charge balance associated with single doping of Nb^{5+} ions can only be achieved through generating an equal concentration of reduced Ti^{3+} ions.

Experimentally, we find that nearly all of the Nb^{5+} ions in the initial reaction solution can be doped into anatase TiO_2 nanocrystals (**Figure 1**a). Their doping concentrations are thus easily controlled through just tuning the added weight of starting materials like niobium pentachloride. By contrast, only a small proportion of In^{3+} ions in the reaction solution can be finally incorporated into TiO_2 to achieve a closely equivalent doping level as that of the Nb^{5+} ions (Figure 1b). For example, if ~5.0 at.% In^{3+} ions (compared to total titanium ions, *i.e.* $y \approx 0.046$ in the above chemical formula) are designed in co-doped TiO_2 nanocrystals, their actual concentration in the initial reaction solution should be up to ~90 at.%. Most of the In^{3+} ions are left in the reaction solution and should be further separated from the synthesized nanoparticles through post-treatment process for reuse.

In addition, we further found that the doping level of Nb^{5+} ions in the co-doped TiO_2 nanocrystals remained virtually unchanged for reaction times between 4 h and 14 h while that of the In^{3+} ions increases almost linearly over the same reaction period (Figure 1c). For reaction times shorter than 4 h, it is dif-

ficult to collect any nanoparticles from the viscous and transparent reaction solution. In such short reaction times, nanoparticles perhaps are not formed or their particle size is too small to be separated for collection. After 14 h, the ratio of In/Ti and Nb/Ti in the nanocrystals does not obviously change. Clearly, the incorporation of Nb^{5+} ions is related to a typical nucleation doping. Though the major proportion of the doped In^{3+} ions (~4.1 at.%, compared to total titanium ions) is also introduced together with Nb^{5+} ions through nucleation doping, the remaining proportion of them (~0.9 at.%) is actually incorporated into TiO_2 through diffusion doping with a diffusion rate of ~$9.52x10^{-4}$ molar per hour. Dual mechanisms (nucleation and diffusion doping) are thus proposed for the introduction of the In^{3+} ions and nucleation-only doping is suggested for that of the Nb^{5+} ions. This understanding of doping mechanisms is critical for the controllable synthesis of other metal ion co-doped nanomaterials and the desirable design of material properties.[20-22]

A schematic, which visually illustrates the two mechanisms of introducing In^{3+} and Nb^{5+} ions into TiO_2 nanocrystals, is shown in Figure 1d. Three critical steps are involved during synthesis, *i.e.* (1) homogeneous distribution of all cations (Ti^{4+}, Nb^{5+} and In^{3+}) in the ethanol solvent to form one transparent solution; (2) the non-equivalent nucleation co-doping of almost all of the Nb^{5+} ions but only a proportion of the In^{3+} ions, which results in the lower doping concentrations of the In^{3+} ions relative to that of the Nb^{5+} ions; and (3) the diffusion doping of an additional proportion of In^{3+} ions to achieve equivalent doping levels of the In^{3+} and Nb^{5+} ions. It seems that the easy Nb^{5+} dopant ions create a synergistic environment for accommodating the more difficult In^{3+} dopant ions. The coupling of these two different types of doped ions is thus demonstrated to be an efficient method to significantly increase the doping concentration of difficult-dopants.

The synthesized (In^{3+}+Nb^{5+}) co-doped TiO_2 nanocrystals were then investigated by X-ray powder diffraction (XRD). All diffraction peaks could be assigned to an average tetragonal anatase-type phase with space group symmetry $I4_1/amd$ (SI-4, supporting information). This phase analysis was carefully done to be sure that all other analyses were conducted on the single phase sample. The chemical compositions of the optimized, co-doped anatase nanocrystals were then carefully analyzed via energy dispersive X-ray spectroscopy (EDS) in a scanning electron microscope (SEM) and an inductively coupled plasma optical emission spectrometer (ICP-OES). The atomic ratio of indium to niobium is found to be about 1:1 and their respective doping concentrations nearly approach 0, 1.0, 3.0 and 4.6 at.%, *i.e.* y≈z≈0, 0.010, 0.030 and 0.046 (SI-5, supporting information). With the gradual increase in the y and z values, there is a gradual shift of the (101) XRD peak, a linear expansion of the lattice parameters (***a***, ***b*** and ***c***) and of the unit cell volume (***V***, SI-4, supporting information) due to the partial substitution of the smaller Ti^{4+} ions with the bigger In^{3+} and Nb^{5+} ions. These XRD results and the various microscopic characterization (to be discussed below) suggest the effective co-doping of In^{3+} and Nb^{5+} ions into anatase TiO_2 nanoparticles. This is also confirmed by Raman spectra which exhibit similar Raman peaks to the un-doped anatase TiO_2 nanoparticles (SI-6, supporting information).[23] Furthermore, we do not detect any other Raman signals or additional XRD peaks even in the samples with y≈z≈0.046 (*i.e.* a total doping concentration of ~9.2 at.%) and thus believe that these (In^{3+}+Nb^{5+}) co-doped TiO_2 nanocrystals represent a single phase solid solution.

The chemical valence states of the cations in the co-doped nanocrystals with y≈z≈0.046 were subsequently analyzed by X-ray photoelectron spectroscopy (XPS, **Figure 2**a, 2b and 2c). As seen, the indium and niobium ions have the chemical valence of +3 and +5, respectively, *i.e.* their chemical valences are the same as those of their starting materials. For the titanium ions, the XPS data show two separate peaks with individual binding energies of ~459.3 and 457.6 eV. These two XPS peaks correspond to Ti^{4+} and Ti^{3+}, respectively. The generation of Ti^{3+} ions can be ascribed to the reduction of a proportion of the Ti^{4+} ions induced by the Nb^{5+} ions. Their concentration is calculated to be ~3.5 at.% by fitting to the XPS data (Figure 2c). The slight difference between the doping level of Ti^{3+} (3.5 at.%) and that of the Nb^{5+} ions (4.6 at.%) is attributed to the oxidization of partial surficial Ti^{3+} ions due to the high surface energy and high reaction activity of the nanoparticles. The presence of Ti^{3+} ions is also confirmed by the electron paramagnetic resonance (EPR) spectrum (Figure 2d). Two EPR signals at g_1=1.97 and g_2=1.94 should come from the paramagnetic resonances of Ti^{3+} with $3d^1$ electrons trapped on the lattices.[24] There is no Nb^{4+} observed in both XPS and EPR characterization. The prepared (In^{3+}+Nb^{5+}) co-doped TiO_2 nanocrystals thus not only contain In^{3+} and Nb^{5+} co-dopants but also include induced Ti^{3+} ions and oxygen vacancies (to balance the charge of the overall co-doped TiO_2 material). The In^{3+}, Nb^{5+}, Ti^{3+} and oxygen vacancies are labelled $In_{Ti}^{'}$, $Nb_{Ti}^{\bullet}$, $Ti_{Ti}^{'}$ and $V_O^{\bullet\bullet}$ using Kröger-Vink notation, respectively.

To further investigate In^{3+} and Nb^{5+} co-doped TiO_2 nanocrystals, aberration-corrected HAADF-STEM (high-angle annular dark-field scanning transmission electron microscopy) images of the synthesized $(Ti^{4+}_{0.862}Ti^{3+}_{0.046}In^{3+}_{0.046}Nb^{5+}_{0.046})(O^{2-}_{1.977}\square_{0.023})$ nanocrystals *(i.e.* x≈y≈z≈0.046) were taken (**Figure 3)**. It is observed that most of the nanocrystals have quasi-spherical shapes (in projection) with small average particle diameters of less than 10 nm. In atomic resolution HAADF-STEM mode, an atomic column containing any indium (atomic number, Z=49) and/or niobium atoms (Z=41) substituting for the lighter Ti atoms (Z=22) should lead to a noticeable local increase in the corresponding image intensity relative to a pure, unsubstituted Ti column (of the same thickness). The inset in Figure 3 shows a HAADF-STEM image of a nanoparticle exhibiting (011) lattice fringes (running vertically). The alternating bright and dark stripes correspond to double rows of metal ions (separated in the horizontal direction by 0.88 Å, and clearly unresolved) and the complete absence of metal ions, respectively. Note that the arrowed bright dots in the inset always fall within the bright metal ion striped regions, suggesting that they represent local atomic columns with an increased density of substituted In and Nb atoms. Indeed, they may well represent individual In or Nb atoms. This directly demonstrates that In^{3+} and Nb^{5+} ions are indeed co-doped into the crystal structures of anatase nanocrystals. In addition, the results of element mapping also indicate that In^{3+} and Nb^{5+} ions are really co-doped into anatase TiO_2 nanocrystals and homgenrously distributed (SI-7, supporting information).

It also appears that most of the quasi-spherical nanocrystals achieved at the higher doping levels gradually evolve to nanocubes or nanocuboids with a decrease in the co-dopant concentration (SI-7, supporting information), consistent with results reported for Nb mono-doped TiO_2[19] and Mg mono-doped ZnO[25] nanoparticles and can be attributed to their changed local crystal structure after co-doping (SI-4, supporting information).

Additionally, the change of co-doping concentration slightly modified the average particle size and higher doping levels lead to smaller particle diameters, but they all remain less than 10 nm both in terms of the size calculated by the Scherrer equation[26,27] and that estimated via low magnification TEM lattice imaging (SI-8, supporting information). These small nanoparticles potentially provide many practical applications, *e.g.* to prepare thin films by directly depositing them onto substrates, use as building blocks in constructing functional nanodevices or to lower the sintering temperatures of related ceramics as raw materials/additives.

In order to gain further insight into possible local defect clusters created by the co-doping of In^{3+} and Nb^{5+} ions, DFT calculations were carried out on our synthesized anatase compounds with the chemical formula of $(Ti^{4+}_{0.862}Ti^{3+}_{0.046}In^{3+}_{0.046}Nb^{5+}_{0.046})(O^{2-}_{1.977}\square_{0.023})$. The calculations were performed using the VASP code[28-31] and a 3×3×1 supercell of the anatase TiO_2 structure. Four Ti^{4+} ions were substituted by two In^{3+} and two Nb^{5+} ions in various configurations. This yielded a respective doping level of 5.56 at.%, which is very close to the experimental value (4.6 at.% In^{3+}+4.6 at.% Nb^{5+}) of this work. More details about the calculation setup are given in SI-9 (supporting information).

The total energy of the co-doped compounds is found to depend strongly on the configuration of the substituted ions. The lowest energy defect structure is provided by the configuration shown in **Figure 4**. The $2In'_{Ti}+V_O^{\bullet\bullet}+Ti'_{Ti}$ "triangle" motif, which was previously identified in the (In^{3+}+Nb^{5+}) co-doped rutile TiO_2,[1] was also observed here. This configuration was characterized by In^{3+} ions located in adjacent octahedra, with one of the shared oxygen ions removed for local charge balance considerations. A Nb^{5+} ion would be in a nearby octahedron such that a Ti ion across the oxygen vacancy from the indium ions was reduced to Ti^{3+}. In the low energy configurations, one Nb^{5+} ion is connected to the triangular-shaped defect cluster to form a more complicated $2In'_{Ti}+V_O^{\bullet\bullet}+Ti'_{Ti}+Nb^{\bullet}_{Ti}$ defect complex. The other Nb^{5+} ion links with the second Ti^{3+} ion to form a $Ti'_{Ti}+Nb^{\bullet}_{Ti}$ defect pair. This defect pair would be located nearby within the supercell, with the lowest energies found when it was adjacent to the $2In'_{Ti}+V_O^{\bullet\bullet}+Ti'_{Ti}+Nb^{\bullet}_{Ti}$ defect clusters. Although these defect models also contain triangle-shaped defect complexes and are thus similar to that of (In^{3+}+Nb^{5+}) co-doped rutile TiO_2,[1] they also exhibit their own special features with (1) the newly introduced $Ti'_{Ti}+Nb^{\bullet}_{Ti}$ defect pairs which may be nearby but not adjacent to the triangular In-containing defect clusters; and (2) the triangle-shaped defect complexes is modified by one Nb^{5+} ion to form a more complicated $2In'_{Ti}+V_O^{\bullet\bullet}+Ti'_{Ti}+Nb^{\bullet}_{Ti}$ defect cluster. Two polymorphs of a single material can thus locally produce different defect models though the selected co-dopants are the same.

Figure 5 presents the high-pressure reaction behaviour of these defect-cluster and defect-pair modified nanocrystals with x≈y≈z ≈0.010. *In situ* Raman signals were collected under compression and decompression conditions. Detailed experimental processes are described in SI-10 (supporting information). A gradual phase transition from anatase to a baddeleyite-like structure can be observed under compression (Figure 5a). Subsequently, the newly formed baddeleyite-like structure transforms to an α-PbO_2-like phase under decompression (Figure 5b). During the entire compression and decompression cycle, the co-doped anatase nanocrystals undergo an anatase → baddeleyite-like phase (~20.2 GPa, compression) → α-PbO_2-like structure (~33.0 GPa, decompression) phase transition sequence. This structural transition sequence is inconsistent with the pressure-induced amorphisation of un-doped anatase TiO_2 nanocrystals having a similar crystal size,[32-35] but is closely analogous to the phase transition behavior of those pure TiO_2 nanocrystals with a larger particle size of 11 to 40 nm.[36-38] The anatase $(Ti^{4+}_{1-x-y-z}Ti^{3+}_{x}In^{3+}_{y}Nb^{5+}_{z})(O^{2-}_{2-(x+y-z)/2}\square_{y/2})$ nanocrystals thus possess an abnormal trans-regime structural transition behaviour under high pressure. This abnormal phase evolution should be related to the intentionally introduced $2In'_{Ti}+V_O^{\bullet\bullet}+Ti'_{Ti}+Nb^{\bullet}_{Ti}$ defect clusters and/or $Ti'_{Ti}+Nb^{\bullet}_{Ti}$ defect pairs since they can act as nucleation centers of baddeleyite- or α-PbO_2-like metastable polymorphic phases and thus induce the crystallization of new crystal structures.

In conclusion, highly concentrated In^{3+} difficult-dopants are successfully introduced into TiO_2 crystal structures through the synergistic effects of the Nb^{5+} easy-dopants. It is found that the dual mechanisms of nucleation and diffusion doping are responsible for the incorporation of the difficult-dopant In^{3+} ions while nucleation-only doping is observed for that of the easy-dopant Nb^{5+} ions. The local defect structures generated by co-doped In^{3+}, Nb^{5+} ions, their resultant Ti^{3+} and oxygen vacancies are composed of both $2In'_{Ti}+V_O^{\bullet\bullet}+Ti'_{Ti}+Nb^{\bullet}_{Ti}$ defect clusters and equivalent $Ti'_{Ti}+Nb^{\bullet}_{Ti}$ defect pairs. These intentionally introduced defects would act as nucleation centers of baddeleyite- and α-PbO_2-like metastable polymorphic phases and thereby induce an abnormal trans-regime structural transition of co-doped anatase TiO_2 nanocrystals under high pressure. We believe that this work provides new insight into the design and synthesis of other novel co-doped materials with high concentrations of difficult-dopant ions, opens a new avenue to develop new co-doping systems for developing new functional materials, and significantly advances local defect structures in solids.

ASSOCIATED CONTENT

Supplementary materials about the synthesis and characterization of $(Ti^{4+}_{1-x-y-z}Ti^{3+}_{x}In^{3+}_{y}Nb^{5+}_{z})(O^{2-}_{2-(x+y-z)/2}\square_{y/2})$ anatase nanocrystals, the analysis of their chemical compositions, average particle size and other related properties are available in the supporting information (SI).

AUTHOR INFORMATION

Corresponding Author
*yun.liu@anu.edu.au and **t.frankcombe@adfa.edu.au

Author contributions
Q. S., R. L. W., Y. L. and T. J. F. make the main contribution to the preparation of this manuscript. Y. L. initiated this research, planned and coordinated all experimental and theoretical work. T. J. F. did the theoretical work collaborated with Y. L. Q. S. designed the approach for the fabrication of the samples with different compositions and synthetic conditions. Q. S., H. C., L. N. and R. L. W. conducted HRTEM, SEM/EDS, XPS analysis. C. Z. and J. E. conducted the measurement of high-angle annular dark-field scanning transmission electron microscopy. Q. S. and L. Q. H. performed the high-pressure reaction experiments under the supervision of J. E. B. All authors were involved in the data analysis and discussion as well as the manuscript preparation.

Competing financial interests
The authors declare no competing financial interest.

ACKNOWLEDGMENT

Q. S., Y. L. and T. J. F. acknowledge the supports of the Australian Research Council (ARC) in the form of Discovery Projects. Y. L., T. J. F. and J. E. B. also appreciate the support from the ARC Future Fellowships program. The authors acknowledge the facilities and the scientific and technical assistance of the Australian microscopy and microanalysis research facility (AMMRF) at the Centre of advanced Microscopy, the Australian National University. The authors also appreciate Jie Gao (Shanghai Institute of Ceramics) for her assistance in ICP-OES analysis and Bill Gong (University of New South Wales) for his help in XPS characterization. The FEI Titan3 80-300 S/TEM instrument at the Monash Centre for Electron Microscopy was funded by ARC Grant LE0454166.

REFERENCES

[1] Hu, W.; Liu, Y.; Withers, R. L.; Frankcombe, T. J.; Norén, L.; Snashall, A.; Kitchin, M.; Smith, P.; Gong, B.; Chen, H.; *et al.* Electron-pinned defect-dipoles for high-performance colossal permittivity materials. *Nat. Mater.* **2013**, *12*, 821-826.

[2] Liu, G.; Yin, L. -C.; Wang, J.; Niu, P.; Zhen, C.; Xie, Y.; Chen, H. -M. A red anatase TiO_2 photocatalyst for solar energy conversion. *Energy Environ. Sci.* **2012**, *5*, 9603-9610.

[3] Zarhri, Z.; Benyoussef, A.; Kenz, A. E. Theoretical study of TiO_2 doped with single and double impurities. *J. Supercond. Nov. Magn.* **2014**, *27*, 1323-1328.

[4] Ito, Y.; Cong, W.; Fujita, T.; Tang, Z.; Chen, M. High catalytic activity of nitrogen and sulfur co-doped nanoporous graphene in the hydrogen evolution reaction. *Angew. Chem. Int. Ed.* **2015**, *54*, 2131-2136.

[5] Zhao, Y.; Yang, L.; Chen, S.; Wang, X.; Ma, Y.; Wu, Q.; Jiang, Y.; Qian, W.; Hu, Z. Can boron and nitrogen co-doping improve oxygen reduction reaction activity of carbon nanotubes? *J. Am. Chem. Soc.* **2013**, *135*, 1201-1204.

[6] Wu, P.; Yan, X. -P. Doped quantum dots for chemo/biosensing and bioimaging. *Chem. Soc. Rev.* **2013**, *42*, 5489-5521.

[7] Lu, X.; Morelli, D. T.; Xia, Y.; Ozolins, V. Increasing the thermoelectric figure of merit of tetrahedrites by co-doping with nickel and zinc. *Chem. Mater.* **2015**, *27*, 408-413.

[8] Atanacio, A. J.; Bak, T.; Nowotny, J. Effect of indium segregation on the surface versus bulk chemistry for indium-doped TiO_2. *ACS Appl. Mater. Interfaces* **2012**, *4*, 6626-6634.

[9] Rumaiz, A. K.; Woicik, J. C.; Cockayne, E.; Lin, H. Y.; Jaffari, G. H.; Shah, S. I. Oxygen vacancies in N doped anatase TiO_2: experiment and first-principles calculations. *Appl. Phys. Lett.* **2009**, *95*, 262111.

[10] Kong, L.; Wang, C.; Zheng, H.; Zhang, X.; Liu, Y. Defect-induced yellow color in Nb-doped TiO_2 and its impact on visible-light photocatalysis *J. Phys. Chem. C* **2015**, *119*, 16623-16632.

[11] Sun, Q.; Cortie, D.; Zhang, S.; Frankcombe, T. J.; She, G.; Gao, J.; Sheppard, L. R.; Hu, W.; Chen, H.; Zhuo, S.; *et al.* The formation of defect-pairs for highly efficient visible-light catalysts. *Adv. Mater.* **2017**, 29, *1605123*.

[12] Gai, Y.; Li, J.; Li, S. -S.; Xia, J. -B.; Wei, S. -H. Design of narrow-gap TiO_2: a passivated codoping approach for enhanced photoelectrochemical activity. *Phys. Rev. Lett.* **2009**, *102*, 036402.

[13] Breault, T. M.; Bartlett, B. M. Composition dependence of TiO_2:$(Nb,N)_{-x}$ compounds on the rate of photocatalytic methylene blue dye degradation. *J. Phys. Chem. C* **2013**, *117*, 8611-8618.

[14] Dong, W.; Hu, W.; Berlie, A.; Lau, K.; Chen, H.; Withers, R. L.; Liu, Y. Colossal dielectric behavior of Ga+Nb co-doped rutile TiO_2. *ACS Appl. Mater. Interfaces* **2015**, *7*, 25321-25325.

[15] Hu, W.; Lau, K.; Liu, Y.; Withers, R. L.; Chen, H.; Fu, L.; Gong, B.; Hutchison, W. Colossal dielectric permittivity in (Nb+Al) codoped rutile TiO_2 ceramics: compositional gradient and local structure. *Chem. Mater.* **2015**, *27*, 4934-4942.

[16] Brown, I. D. Chemical and steric constraints in inorganic solids. *Acta Cryst.* B **1992**, *48*, 553-572.

[17] Brown, I. D. Influence of chemical and spatial constraints on the structures of inorganic compounds. *Acta Cryst.* B **1997**, *53*, 381-393.

[18] For the detailed Bond Valence Sum calculation, please see http://www.softbv.net/indexconv.html.

[19] Trizio, L. D.; Buonsanti, R.; Schimpf, A. M.; Llordes, A.; Gamelin, D. R.; Simonutti, R.; Milliron, D. J. Nb-doped colloidal TiO_2 nanocrystals with tunable infrared absorption. *Chem. Mater.* **2013**, *25*, 3383-3390.

[20] Norris, D. J.; Efros, A. L.; Erwin, S. C. Doped nanocrystals. *Science* **2008**, *319*, 1776-1779.

[21] Buonsanti, R.; Milliron, D. J. Chemistry of doped colloidal nanocrystals. *Chem. Mater.* **2013**, *25*, 1305-1317.

[22] Vlaskin, V. A.; Barrows, C. J.; Erickson, C. S.; Gamelin, D. R. Nanocrystal diffusion doping. *J. Am. Chem. Soc.* **2013**, *135*, 14380-14389.

[23] Naldoni, A.; Allieta, M.; Santangelo, S.; Marelli, M.; Fabbri, F.; Cappelli, S.; Bianchi, C. L.; Psaro, R.; Santo, V. D. Effect of nature and location of defects on bandgap narrowing in black TiO_2 nanoparticles. *J. Am. Chem. Soc.* **2012**, *134*, 7600-7603.

[24] Khomenko, V. M.; Langer, K.; Rager, H.; Fett, A. Electronic absorption by Ti^{3+} ions and electron delocalization in synthetic blue rutile. *Phys. Chem. Miner.* **1998**, *25*, 338-346.

[25] Yang, Y.; Jin, Y.; He, H.; Wang, Q.; Tu, Y.; Lu, H.; Ye, Z. Dopant-induced shape evolution of colloidal nanocrystals: the case of zinc oxide. *J. Am. Chem. Soc.* **2010**, *132*, 13381-13394.

[26] Folli, A.; Pochard, I.; Nonat, A.; Jakobsen, U. H.; Shepherd, A. M.; Macpheez, D. E. Engineering photocatalytic cements: understanding TiO_2 surface chemistry to control and modulate photocatalytic performances. *J. Am. Ceram. Soc.* **2010**, *93*, 3360-3369.

[27] Sun, Q.; Zeng, Y. -P.; Jiang, D. High magnetic field inducing magnetic transitions of Fe^{3+} and Ni^{2+} doped In_2O_3 nanocubes. *Solid State Commun.* **2011**, *151*, 1220-1205.

[28] Kresse, G.; Hafner, J. Ab initio molecular dynamics for liquid metals. *Phys. Rev. B* **1993**, *47*, 558.

[29] Kresse, G.; Furthmüller, J. Efficient iterative schemes for ab initio total-energy calculations using a plane-wave basis set. *Phys. Rev. B* **1996**, *54*, 11169-11184.

[30] Hacene, M.; Anciaux-Sedrakian, A.; Rozanska, X.; Klahr, D.; Guignon, T.; Fleurat-Lessard P. Accelerating VASP electronic structure calculations using graphic processing units. *J. Comput. Chem.* **2012**, *33*, 2581-2589.

[31] Hutchinson, M.; Widom, M. VASP on a GPU: application to exact-exchange calculations of the stability of elemental boron. *Comput. Phys. Commun.* **2012**, *183*, 1422-1426.

[32] Wang, Z.; Saxena, S. K. Raman spectroscopic study on pressure-induced amorphization in nanocrystalline anatase (TiO_2). *Solid State Commun.* **2001**, *118*, 75-78.

[33] Dubrovinskaia, N. A.; Dubrovinsky, L. S.; Ahuja, R.; Prokopenko, V. B.; Dmitriev, V.; Weber, H. -P.; Osorio-Guillen, J. M.; Johansson, B. Experimental and theoretical identification of a new high-pressure TiO_2 polymorph. *Phys. Rev. Lett.* **2001**, *87*, 275501.

[34] Pischedda, V.; Hearne, G. R.; Dawe, A. M.; Lowther, J. E. Ultrastability and enhanced stiffness of ~ 6 nm TiO_2 nanoanatase and eventual pressure-induced disorder on the nanometer scale. *Phys. Rev. Lett.* **2006**, *96*, 035509.

[35] Swamy, V.; Kuznetsov, A.; Dubrovinsky, L. S.; McMillan, P. F.; Prakapenka, V. B.; Shen, G.; Muddle, B. C. Size-dependent pressure-induced amorphization in nanoscale TiO_2. *Phys. Rev. Lett.* **2006**, *96*, 135702.

[36] Hearne, G. R.; Zhao, J.; Dawe, A. M.; Pischedda, V.; Maaza, M.; Nieuwoudt, M. K.; Kibasomba, P.; Nemraoui, O.; Comins, J. D. Witcomb, M. J. Effect of grain size on structural transitions in anatase TiO_2: a Raman spectroscopy study at high pressure. *Phys. Rev. B* **2004**, *70*, 134102.

[37] Swamy, V.; Kuznetsov, A.; Dubrovinsky, L. S.; Caruso, R. A.; Shchukin, D. G.; Muddle, B. C. Finite-size and pressure effects on the Raman spectrum of nanocrystalline anatase TiO_2. *Phys. Rev. B* **2005**, *71*, 184302.

[38] Swamy, V.; Dubrovinsky, L. S.; Dubrovinskaia, N. A.; Simionovici, A. S.; Drakopoulos, M.; Dmitriev, V.; Weber, H. -P. Compression behavior of nanocrystalline anatase TiO_2. *Solid State Commun.* **2003**, *125*, 111-115.

Figures

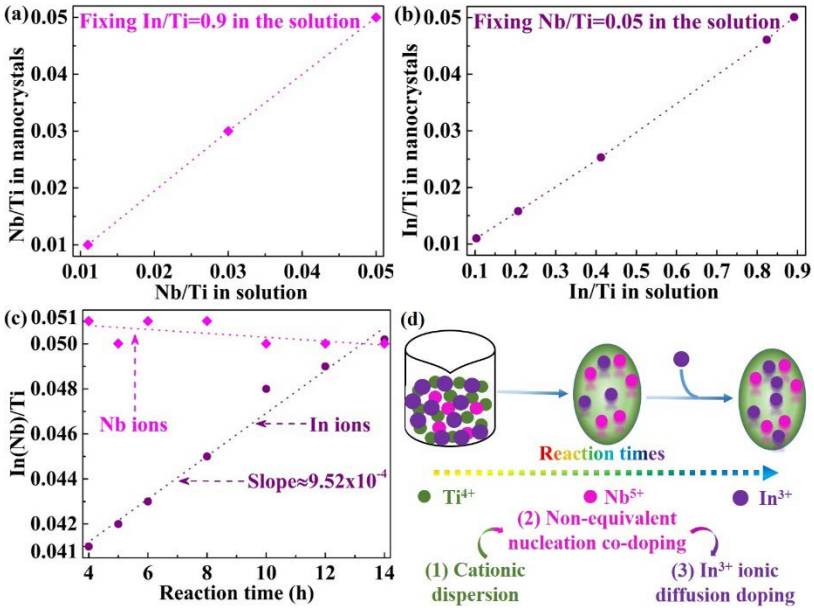

Figure 1. The ratio of Nb/Ti (a) and In/Ti (b) in the initial reaction solution (x axis) and in the resultant co-doped anatase TiO_2 nanocrystals (y axis). These data points were collected at the reaction time of 14 h. It is found that almost all of the Nb ions but only a small proportion of the In ions in the reaction solution can be finally co-doped into TiO_2. (c) is the ratio of Nb/Ti and In/Ti at different reaction times, suggesting that dual mechanisms of nucleation and diffusion doping are responsible for the incorporation of the In^{3+} ions while nucleation-only doping is observed for that of the Nb^{5+} ions. (d) is a schematic illustrating the different doping mechanisms for the In^{3+} and Nb^{5+} co-dopants. Three critical steps should be involved during the synthesis: (1) cationic homogeneous distribution in the solution; (2) non-equivalent nucleation co-doping of Nb^{5+} and In^{3+} ions; and (3) the further diffusion doping of the In^{3+} ions to achieve the equal doping concentrations as that of the Nb^{5+} ions.

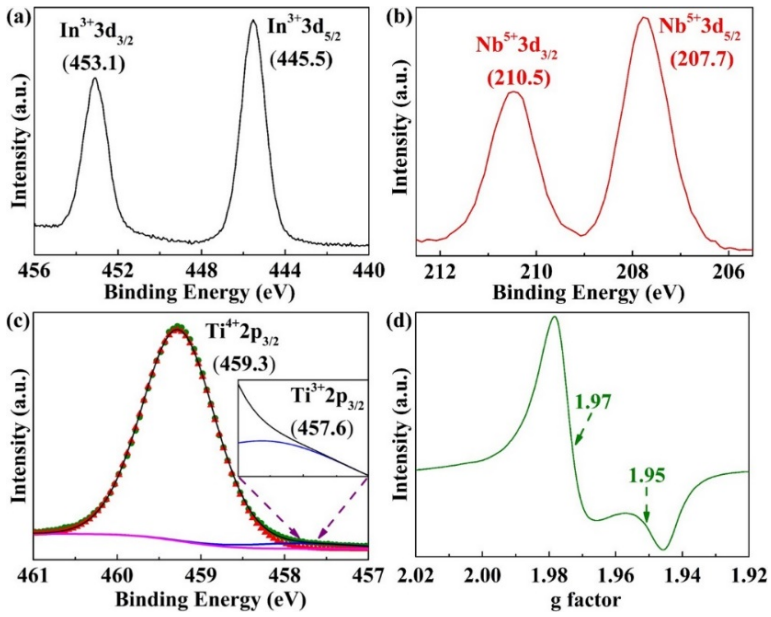

Figure 2. The XPS (a-c) and room temperature EPR (d) spectra of the synthesized $(Ti^{4+}_{0.862}Ti^{3+}_{0.046}In^{3+}_{0.046}Nb^{5+}_{0.046})(O^{2-}_{1.977}\square_{0.023})$ anatase nanocrystals with x≈y≈z≈0.046, determining the chemical valence states of indium (+3) and niobium (+5) co-dopants as well as the titanium (+4 and +3).

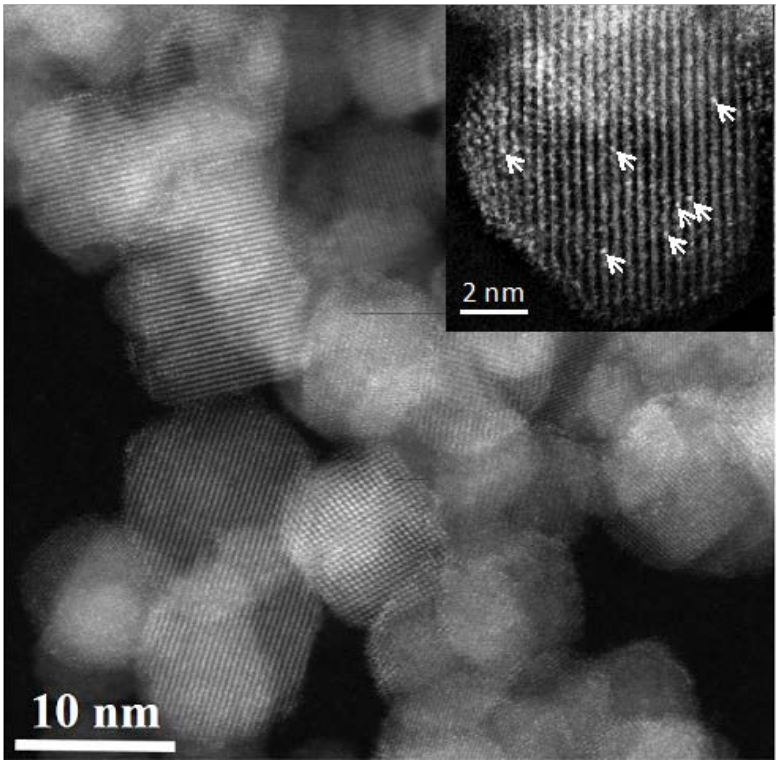

Figure 3. A typical aberration-corrected HAADF-STEM image of the synthesized anatase ($Ti^{4+}_{0.862}Ti^{3+}_{0.046}In^{3+}_{0.046}Nb^{5+}_{0.046}$)($O^{2-}_{1.977}\square_{0.023}$) nano-crystals with x≈y≈z≈0.046. The arrowed brighter dots in the inset show the presence of atomic columns with a greater density of heavier atoms (indium and/or niobium), indicating that the In^{3+} and Nb^{5+} ions are indeed co-doped into TiO_2 host materials.

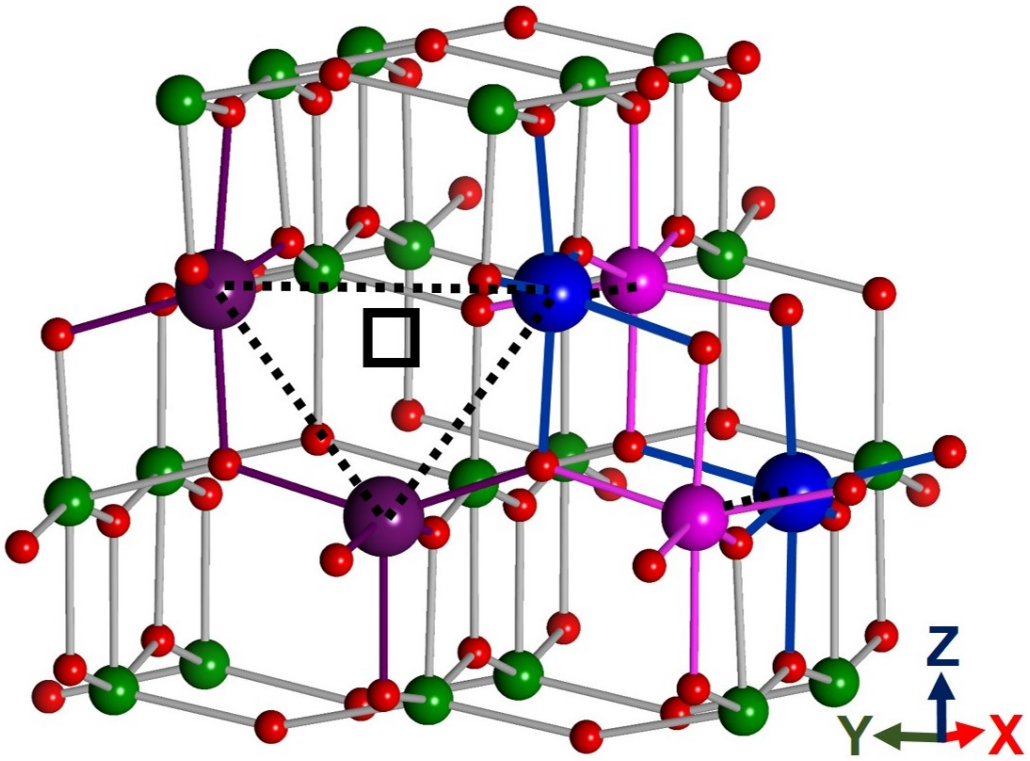

Figure 4. The motif of the lowest energy defect structures. Balls representing ions are colored according to In^{3+}: purple; Nb^{5+}: pink; Ti^{3+}: blue; Ti^{4+}: green; O^{2-}: red. Dashed lines indicate the $2In'_{Ti}+V^{\bullet\bullet}_{O}+Ti'_{Ti}+Nb^{\bullet}_{Ti}$ defect clusters and adjacent $Ti'_{Ti}+Nb^{\bullet}_{Ti}$ defect pairs.

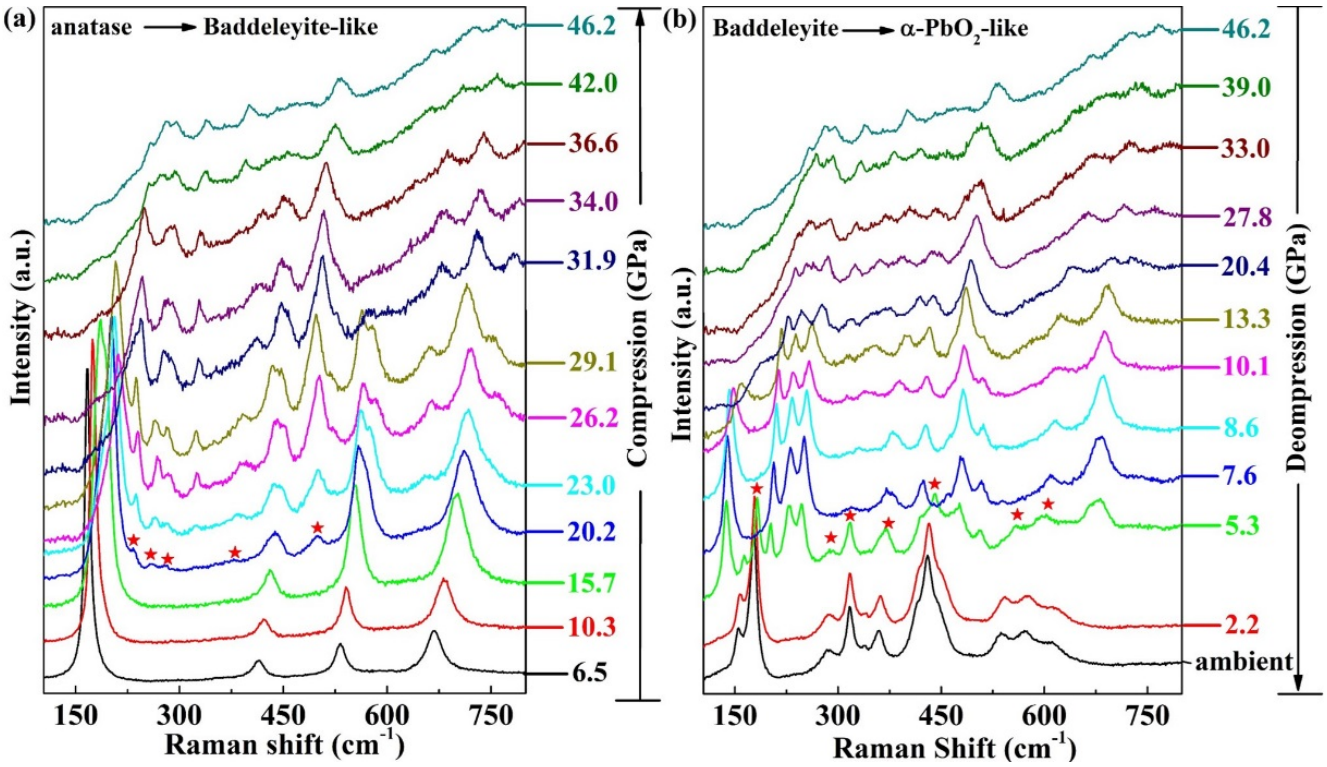

Figure 5. *In situ* Raman spectra of anatase ($Ti^{4+}_{0.970}Ti^{3+}_{0.010}In^{3+}_{0.010}Nb^{5+}_{0.010}$)($O^{2-}_{1.995}\square_{0.005}$) nanocrystals (x≈y≈z≈0.010) collected under compression (a) and decompression (b) conditions. Their crystallographic evolution follows the sequence of anatase → baddeleyite-like phase (compression) → α-PbO_2-like structure (decompression).